J. Comput. Phys. **229** (2010) 498–511, doi:10.1016/j.jcp.2009.09.039

3D Phase-Field Simulations of Interfacial Dynamics in Newtonian and Viscoelastic Fluids

Chunfeng Zhou[1*], Pengtao Yue[2], James J. Feng[1,3†] Carl F. Ollivier-Gooch[4], Howard H. Hu[5]

[1] *Department of Chemical and Biological Engineering, University of British Columbia, Vancouver, BC V6T 1Z3, Canada*

[2] *Department of Mathematics, Virginia Polytechnic Institute and State University, Blacksburg, VA 24061, USA*

[3] *Department of Mathematics, University of British Columbia, Vancouver, BC V6T 1Z2, Canada*

[4] *Department of Mechanical Engineering, University of British Columbia, Vancouver, BC V6T 1Z4, Canada*

[5] *Department of Mechanical Engineering and Applied Mechanics, University of Pennsylvania, Philadelphia, PA 19104, USA*

Abstract - This work presents a three-dimensional finite-element algorithm, based on the phase-field model, for computing interfacial flows of Newtonian and complex fluids. A 3D adaptive meshing scheme produces fine grid covering the interface and coarse mesh in the bulk. It is key to accurate resolution of the interface at manageable computational costs. The coupled Navier-Stokes and Cahn-Hilliard equations, plus the constitutive equation for non-Newtonian fluids, are solved using second-order implicit time stepping. Within each time step, Newton iteration is used to handle the nonlinearity, and the linear algebraic system is solved by preconditioned Krylov methods. The phase-field model, with a physically diffuse interface, affords the method several advantages in computing interfacial dynamics. One is the ease in simulating topological changes such as interfacial rupture and coalescence. Another is the capability of computing contact line motion without invoking ad hoc slip conditions. As validation of the 3D numerical scheme, we have computed drop deformation in an elongational flow, relaxation of a deformed drop to the spherical shape, and drop spreading on a partially wetting substrate. The results are compared with numerical and experimental results in the literature as well as our own axisymmetric computations where appropriate. Excellent agreement is achieved provided that the 3D interface is adequately resolved by using a sufficiently thin diffuse interface and refined grid. Since our model involves several coupled partial differential equations and we use a fully implicit scheme, the matrix inversion requires a large memory. This puts a limit on the scale of problems that can be simulated in 3D, especially for viscoelastic fluids.

[*] Current address: Department of Chemical Engineering and Materials Science, University of Minnesota, Minneapolis, MN 55455, USA.

[†] Corresponding author. E-mail jfeng@CHML.UBC.CA

I. INTRODUCTION

Interfacial dynamics is scientifically intriguing because of the coupling between hydrodynamics in the bulk and deformation of the interfaces. It is also taking on more practical significance with the recent technological advances in microengineering and miniaturization. For example, drop and bubble dynamics has been a key element in designing microfluidic devices [1], where the smaller length scales accentuates the interfacial forces. From a computational standpoint, the moving internal boundaries present a numerical challenge, and two classes of methods have been developed to meet it: interface tracking and interface capturing [2]. The former deploys grid points or markers on the interface that track it each time step [3–5]. The latter uses an auxiliary scalar field that distinguishes the fluid components. Thus, the onus of managing a moving grid is replaced by that of computing a convection or convection-diffusion equation for the scalar field, typically on an Eulerian grid. Each approach has its advantages and limitations.

The phase-field method to be discussed in this paper is an interface-capturing method. It is distinguished from other methods in its class by having a physical origin in a diffuse interface where the two fluid components mix to a limited extent and store a mixing energy. Thus, the phase-field parameter ϕ has a well defined physical meaning; its profile in the diffuse interface may be related to van der Waals-type of long range forces [6], and the mixing energy gives rise to interfacial tension [7]. Because of its energy-based formalism and the physical picture of the diffuse-interface model, it has some unique features among interface-capturing methods [8]: (i) The evolution of the interface is self-consistent and requires no ad hoc intervention such as the re-initialization in level set methods. (ii) The theory has an energy law that ensures well-posedness in numerical computation [9, 10]. (iii) The variational framework easily integrates interfacial treatment and non-Newtonian rheology, as the latter is almost always derivable from a microstructural free energy [11]. (iv) It regularizes singular events on the interfaces such as breakup [12], coalescence [6] and moving contact lines [13, 14].

In recent years, several groups have successfully applied the phase-field method to two-phase flow simulations [7,15–18, e.g.]. These computations demonstrated that for the results to be quantitatively accurate, two conditions have to be met. First, the interface should

be sufficiently thin so that the theoretical model approaches the so-called sharp-interface limit [19]. Second, this thin region must be adequately resolved by fine mesh; it typically requires some 10 grid points. Otherwise, the interfacial layer is subject to unphysical distortions, the interfacial tension is inaccurate and the results are unreliable. Thus, interfacial resolution is the bottleneck for phase-field computations. To address this issue, we have developed AMPHI, a finite-element algorithm on an unstructured grid that is adaptively refined and coarsened as the interface moves [20]. It has been applied so far to drop-interface partial coalescence [21], drop formation in microfluidic channels [12], cell motion in capillary [22], defect dynamics in nematic liquid crystals [23] and defect-mediated self-assembly of microdrops [24]. In particular, we have taken advantage of the variational formalism of the model to incorporate the non-Newtonian rheology of complex fluids.

With a few exceptions [18,25, e.g.], prior phase-field computations are in 2D planar and axisymmetric geometries. In many situations, the two-dimensionality constitutes a serious drawback. Not only are there quantitative differences between 2D and 3D dynamics, as is expected, but they sometimes differ qualitatively. One example is the capillary instability of a thread in 3D contrasted with the stability of a 2D sheet. Besides, the most interesting feature of the physical problem might be accessible only in 3D. For instance, the stratified flow of two fluid components in a pipe is subject to distortion of the interface. A particularly intriguing phenomenon is viscous encapsulation, whereby the less viscous component encircles the more viscous one [26]. In this geometry, a lubrication approximation that ignores the variation along the axis of the pipe will decouple the shear of the primary flow and the secondary flow in the cross-section that would distort the interface [27]. Hence, viscous encapsulation in stratified Newtonian fluids can only be probed by fully 3D computations. Finally, applications to engineering problems will inevitably involve complex 3D geometries.

This work represents an extension of the two-dimensional AMPHI to a full 3D version AMPHI3D. It involves upgrading the solver and mesh generation modules to 3D, and properly integrating the two. In this paper, we will describe the theoretical models and computational algorithm, and present solutions of benchmark problems as validation. As before, we are especially interested in interfacial dynamics of complex fluids with non-Newtonian rheology. If our recent 2D computations illustrated the potential of the AMPHI

algorithm, the 3D version promises a broader range of applications, with opportunities to explore intriguing physics in more complex problems.

II. THEORY AND NUMERICAL METHOD

A. Diffuse interface model

The diffuse-interface method as applied to two-phase flows has been described by a number of authors [15,16,28]. Yue *et al.* [7,11] have shown how the model can be extended to non-Newtonian fluids, and developed the AMPHI algorithm in two dimensional geometries based on finite elements with adaptive meshing [20]. The main ideas of the 3D algorithm are close to those in 2D. In this section, we will briefly summarize these ideas and give the governing equations, using the mixture of a Newtonian and an Oldroyd-B fluid as an example. The method accommodates other types of complex fluids such as nematic liquid crystals [11, 23, 24, 29, 30], but we will confine this paper to Newtonian-Newtonian and Newtonian-Oldroyd-B mixtures.

Consider a Newtonian fluid in contact with an immiscible viscoelastic Oldroyd-B fluid. Their interface may intersect a solid wall to produce a three-phase contact line. The moving contact line presents a well-known stress singularity, and the diffuse interface provides a particularly attractive regularization scheme. Thus, we will include the contact line in the general formulation, and compute the spreading drop as one of the benchmark problems. In the diffuse interface framework, the Newtonian and Oldroyd-B components mix to some extent in a very thin interfacial region and store a mixing energy f_{mix}. In addition, each component interacts with the solid substrate with a fluid-solid surface energy f_w. An Oldroyd-B fluid is a dilute suspension of polymer chains, modeled as linear Hookean dumbbells, in a Newtonian solvent [31]. Thus, there is a bulk energy f_d in the Oldroyd-B component due to the dumbbells. We introduce a phase-field variable ϕ such that the concentrations of the Oldroyd-B and Newtonian components are $(1+\phi)/2$ and $(1-\phi)/2$, respectively. Now the total free energy f_{total} may be written as:

$$f_{total} = \int_\Omega f_{mix}(\phi, \nabla\phi)\, d\Omega + \int_{\partial\Omega_w} f_w(\phi)\, dA + \int_\Omega f_d\, d\Omega, \tag{1}$$

where Ω and $\partial\Omega_w$ denote the fluid domain and the solid substrate. For the mixing energy, we adopt the familiar Ginzburg-Landau form [32]:

$$f_{mix}(\phi, \nabla\phi) = \frac{1}{2}\lambda|\nabla\phi|^2 + \frac{\lambda}{4\epsilon^2}(\phi^2-1)^2, \tag{2}$$

where λ is the mixing energy density with the dimension of force, and ϵ is a capillary width indicative of the thickness of the diffuse interface. As $\epsilon \to 0$, the ratio λ/ϵ produces the interfacial tension σ in the classical sense [7, 16]:

$$\sigma = \frac{2\sqrt{2}}{3}\frac{\lambda}{\epsilon}. \tag{3}$$

The wall energy in diffuse-interface form [14, 33, 34] is

$$f_w(\phi) = -\sigma\cos\theta_S\frac{\phi(3-\phi^2)}{4} + \frac{\sigma_{w1}+\sigma_{w2}}{2}, \tag{4}$$

where σ_{w1} and σ_{w2} are the fluid-solid interfacial tensions for the two fluids, and they determine the static contact angle θ_S through Young's equation:

$$\sigma\cos\theta_S = \sigma_{w2} - \sigma_{w1}. \tag{5}$$

Finally the free energy of the viscoelastic fluid

$$f_d = \frac{1+\phi}{2}n\int_{R^3}\left(kT\ln\Psi + \frac{1}{2}H\boldsymbol{Q}\cdot\boldsymbol{Q}\right)\Psi d\boldsymbol{Q}, \tag{6}$$

where n is the number density of dumbbells, k is the Boltzmann constant, T is temperature, H is the elastic spring constant, $\Psi(\boldsymbol{Q})$ is the configuration distribution and $\boldsymbol{Q}$ is the vector connecting the ends of the spring [31].

A variational procedure applied to the total free energy yields the stress tensor for the system, with contributions from the elastic springs and the interface. Thus, the equations of motion can be written as:

$$\nabla\cdot\boldsymbol{v} = 0, \tag{7}$$

$$\rho\left(\frac{\partial\boldsymbol{v}}{\partial t} + \boldsymbol{v}\cdot\nabla\boldsymbol{v}\right) = -\nabla p + \nabla\cdot\left[\mu(\nabla\boldsymbol{v} + \nabla\boldsymbol{v}^{\mathrm{T}})\right] + \frac{1+\phi}{2}\nabla\cdot\boldsymbol{\tau}_d + G\nabla\phi + \rho\boldsymbol{g}, \tag{8}$$

where $\rho = \frac{1+\phi}{2}\rho_1 + \frac{1-\phi}{2}\rho_2$, ρ_1 and ρ_2 being the densities for the Oldroyd-B and Newtonian components, and $\mu = \frac{1+\phi}{2}\mu_s + \frac{1-\phi}{2}\mu_n$, μ_s being the viscosity of the Newtonian solvent in the Oldroyd-B component and μ_n the viscosity of the Newtonian component. $G = \frac{\delta\int f_{mix}d\Omega}{\delta\phi} = \lambda\left[-\nabla^2\phi + \frac{\phi(\phi^2-1)}{\epsilon^2}\right]$ is the chemical potential and $\boldsymbol{g}$ is the gravitational acceleration. Note that for simplicity, we have adopted an incompressible formalism, which differs slightly from the quasi-compressible model of Lowengrub and Truskinovsky [15]. The results are unaffected as long as the interface is thin enough for the sharp-interface limit

to be approached. The interfacial stress $G\nabla\phi$ is the diffuse-interface representation of the interfacial force on the fluids [7]. The elastic stress $\boldsymbol{\tau}_d$ due to the dumbbells obeys the Maxwell equation [7,20]:

$$\boldsymbol{\tau}_d + \lambda_H \boldsymbol{\tau}_{d(1)} = \mu_p[\nabla \boldsymbol{v} + (\nabla \boldsymbol{v})^T], \tag{9}$$

where the subscript $_{(1)}$ denotes the upper convected derivative, λ_H is the relaxation time, and μ_p is the polymer viscosity. Finally, the evolution of ϕ is governed by the Cahn-Hilliard equation:

$$\frac{\partial \phi}{\partial t} + \boldsymbol{v} \cdot \nabla \phi = \gamma \nabla^2 G, \tag{10}$$

where γ is the mobility [7]. Equations (7–10) form the governing equations for our two-phase system. For discretization using second-order finite elements, the fourth-order Cahn-Hilliard equation is decomposed into two second-order equations [20,35].

The governing equations are supplemented by the following boundary conditions on the solid wall $\partial\Omega_w$:

$$\boldsymbol{v} = \boldsymbol{v}_w, \tag{11}$$

$$\boldsymbol{n} \cdot \nabla G = 0, \tag{12}$$

$$\lambda \boldsymbol{n} \cdot \nabla \phi + f_w'(\phi) = 0, \tag{13}$$

where $\boldsymbol{v}_w$ is the wall velocity and $\boldsymbol{n}$ is the unit normal to the boundary. The first is the no-slip boundary condition, which implies that the motion of the contact line is solely due to the Cahn-Hilliard diffusion. The second condition is zero flux through the solid wall, which helps conserve the mass for each fluid component. The third is the natural boundary condition from the variation of the wall energy f_w, and $\mathcal{L} = \lambda \boldsymbol{n} \cdot \nabla \phi + f_w'(\phi)$ represents the surface chemical potential. Thus, this condition stipulates that the fluid layer be always at equilibrium with the solid substrate, and the dynamic contact angle remain on the leading order at the static value θ_s [14,33]. Equation (13) can be generalized to account for relaxation of ϕ in the near-wall fluid layer, which will allow the dynamic contact angle to deviate from θ_s. For the simplest case of a constant $f_w = \sigma_{w1} = \sigma_{w2}$, the static contact angle $\theta_s = \pi/2$ and the two fluid components interact equally with the solid substrate. Non-90° contact angles will be specified by a non-constant $f_w(\phi)$.

The AMPHI3D algorithm has the same structure as its 2D precursor: a finite-element flow solver integrated into an adaptive meshing scheme. The former is based on a Navier-Stokes solver that Hu *et al.* [36, 37] have developed for simulating particle motion in Newtonian and viscoelastic fluids, while the latter is based on the mesh generator GRUMMP developed by Ollivier-Gooch and coworkers [38].

B. Numerical implementation

The discretization of the governing equations follows the standard Galerkin formalism [36], and the weak forms of the governing equations are similar to those given by Yue *et al.* [20]. The boundary conditions can be summarized as:

$$\boldsymbol{v} = \boldsymbol{u}, \qquad \text{on } \partial\Omega_u \tag{14}$$

$$(-p\boldsymbol{I} + \boldsymbol{\tau}) \cdot \boldsymbol{n} = 0, \qquad \text{on } \partial\Omega_\tau \tag{15}$$

$$\boldsymbol{\tau}_d = \boldsymbol{\tau}_{in}, \qquad \text{on } \partial\Omega_{in} \tag{16}$$

$$\nabla\phi \cdot \boldsymbol{n} = -\frac{1}{\lambda} f_w'(\phi), \qquad \text{on } \partial\Omega_w \tag{17}$$

$$\nabla(\psi + s\phi) \cdot \boldsymbol{n} = 0, \qquad \text{on } \partial\Omega \tag{18}$$

where $\partial\Omega = \partial\Omega_u \bigcup \partial\Omega_\tau$ and $\partial\Omega_u \bigcap \partial\Omega_\tau = \emptyset$, and $\partial\Omega_{in}$ is the inflow boundary. For stationary walls, $\boldsymbol{u} = 0$. Note that Eq. (17) is a natural boundary condition that is easily incorporated into the finite-element formulation.

For spatial discretization, we use piecewise quadratic (P2) elements for $\boldsymbol{v}$, ϕ and ψ, and piecewise linear (P1) elements for p and $\boldsymbol{\tau}_d$ on an unstructured tetrahedral mesh. For time marching, we use a second-order, fully implicit scheme. The nonlinear algebraic system that results from the finite-element discretization is solved by an inexact Newton's method. Within each Newton iteration, the sparse linear system is solved by preconditioned Krylov methods such as the generalized minimum residual (GMRES) method and the biconjugate gradient stabilized (BCGSTAB) method.

C. Adaptive mesh generation

To achieve high numerical accuracy at a moderate computational cost, we need a mesh with dense grids covering the interfacial region and coarser grids in the bulk. This is particularly important to a diffuse-interface algorithm, since the interface must be thin

enough to attain the sharp-interface limit and yet be adequately resolved for the interfacial forces to be computed accurately. We deploy an Eulerian mesh in space, with a "ribbon" of refined grids covering the interfacial region. As the interface moves out of the fine mesh, the mesh in front is refined while that left behind is coarsened. Such adaptive meshing is achieved by using a general-purpose mesh generator GRUMMP. We have used the 2D version of GRUMMP in our 2D AMPHI algorithm [20], and will summarize the main ideas of GRUMMP and emphasize features unique to 3D meshing. For further details on GRUMMP, interested readers may consult the work of Ollivier-Gooch *et al.* [39, 40]

GRUMMP generates a mesh by using Delaunay refinement, and controls the spatial variation of grid size using a scalar field L_S, which specifies the intended grid size at each location in the domain. In our study of interfacial dynamics, the grid size should be finest in the interfacial region, and gradually coarsens away from the interface. Thus, it is natural to define L_S using the phase-field variable ϕ. The scheme that we previously devised [20] for meshing 2D domains turns out to work equally well for 3D domains:

$$L_S(x, y, z) = \frac{1}{|\nabla\phi|\frac{\sqrt{2}}{C} + \frac{1}{h_\infty}}, \tag{19}$$

where h_∞ is the mesh size in the bulk, and the constant C controls the mesh size in the interfacial region. As ϕ varies between ± 1 across the interface, which has a thickness of several ϵ [7], L_S takes a value $h_1 \approx C \cdot \epsilon$ at the interface. In this paper, we have used C values between 0.5 and 1; results will show that good mesh resolution is achieved with $h_1 \leq \epsilon$. As the diffuse interface has a thickness of roughly 7.5ϵ, it typically comprises some 10 grid points [7, 20]. In addition, the far-field mesh size h_∞ can be set to different values h_2 and h_3 in the two bulk fluids. This will allow, for instance, the interior of a drop to be more finely resolved than the far field of the suspending fluid. In practice, L_S is used in combination with a user-specified "grading factor" that determines how rapidly the grid size increases away from the interface.

GRUMMP produces tetrahedral elements in 3D based on L_S, following the scheme of Shewchuk [41] but with several significant improvements in the areas of cell size and grading control [39]. It begins with enclosing the computational domain Ω inside a large box and implementing an initial tetrahedralization that incorporates all vertices on the domain

boundary $\partial\Omega$ into the mesh. Then tetrahedra outside Ω are discarded. Shewchuk [41] has shown that for common shapes of Ω, the surface $\partial\Omega$ does have a constrained Delaunay tetrahedralization, which means that the surface mesh can be generated. Next, for elements that are too large relative to the local L_S value, and for badly shaped elements, Watson point insertion [42] is performed at the tetrahedral circumcenter. This is implemented by using a priority queue listing all elements based on size and shape. For each tetrahedron, a size measure M_L and a shape measure M_S are computed:

$$M_L = \frac{2}{\sqrt{3}} \cdot \frac{r}{\overline{L_S}}, \tag{20}$$

$$M_S = \frac{\sqrt{6}}{4} \cdot \frac{l_{min}}{r}, \tag{21}$$

where r is the circumradius, l_{min} is the shortest edge of the tetrahedron, and $\overline{L_S}$ is the average of the L_S values on all its vertices. Elements with a larger M_L or a smaller M_S receive higher priority for point insertion. This scheme limits the ratio l_{min}/r to above 0.5 with sufficiently smooth grading, i.e., with gradual spatial variation of the element size. However, in three dimensions, this lower bound on l_{min}/r is not sufficient for eliminating all large-aspect-ratio tetrahedra, which can degrade the accuracy of finite-element solutions of partial differential equations. To address this, the mesh is post-processed by swapping edges and shifting certain vertices. In our experience, this eliminates all poorly shaped tetrahedra from the mesh. Figure 1 shows an example of the mesh inside a cube containing an ellipsoid. Because of symmetry, only one eighth of the physical domain is meshed.

In Fig. 1(b) the interface is covered by a layer of the finest grids. But in dynamic simulations, the interface will in time move out of this layer into coarser grids. Before this happens, GRUMMP is called to refine and coarsen the neighboring regions upstream and downstream of the moving interface, respectively, by point insertion and removal. The solution of the last time step is then projected onto the new grid for time integration. Typically, such remeshing takes place roughly once every 10 time steps. The adaptive coarsening and refinement scheme is similar in principle to the previous 2D implementation, and more details can be found in Yue *et al.* [20] We also use the normal speed of the interface to constrain the time step so that the interface does not advance more than a whole element at one time step.

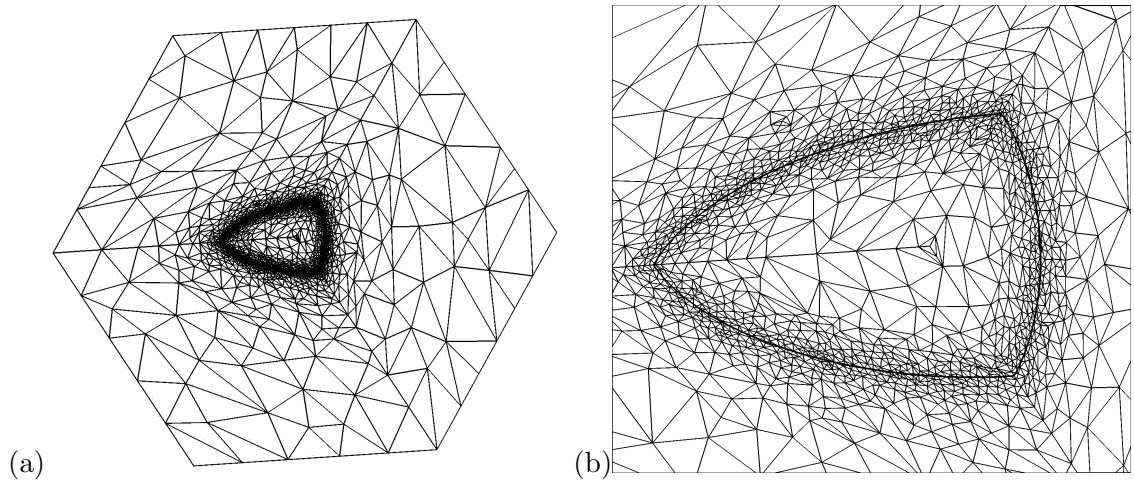

Figure 1: (a) An unstructured tetrahedral mesh generated by GRUMMP with interfacial refinement. For clarity only surface grids on the coordinate planes are drawn. The parameters are: interior mesh size $h_2 = 0.25$, outer boundary mesh size $h_3 = 1$, and interfacial mesh size $h_1 = 0.02$. (b) A magnified view of the interfacial region. The solid curves indicate the ellipsoidal surface.

To a large extent, the size of the mesh limits the magnitude of the problems that can be simulated by AMPHI3D. For instance, the maximum number of tetrahedra for a machine with 10 GB memory is around 150,000. The large memory requirement arises from the fully implicit scheme for solving the Navier-Stokes, Cahn-Hilliard and constitutive equations. On a 3.4 MHz CPU, each time step takes roughly 5 minutes (mostly expended on inverting the linear system), and a typical simulation lasts 10 days.

III. RESULTS AND DISCUSSION

In this section, we will present the numerical results for four problems: drop retraction from an elongated spheroidal initial shape, drop deformation under elongational flow, drop spreading on a partially wetting substrate, and viscoelastic drop retraction. The results are compared with those from the 2D axisymmetric simulations where appropriate as well as those in the literature. It serves to validate the numerical scheme and to demonstrate the capabilities and limitation of our tools. The physical background for the benchmark problems is such that inertia is unimportant in all of them. Thus, this aspect of the code is not probed in this study. We have previously computed axisymmetric flows in which inertia figures prominently [20, 21].

A. Retraction of elongated drop

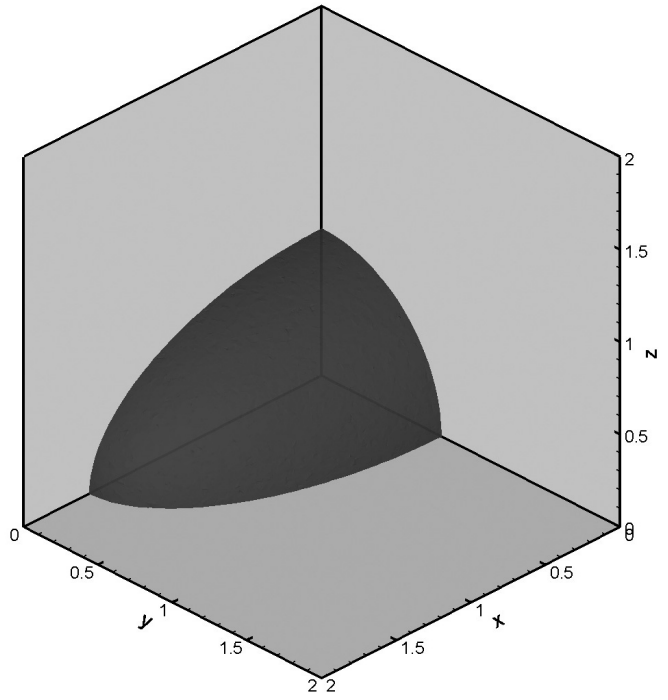

Figure 2: The geometric setup for computing drop retraction. The computational domain is one-eighth of the physical geometry and symmetric boundary conditions are imposed on all three directions. Note that this figure shows only a small proportion of the actual computational domain.

Drop retracting from an elongated initial shape to a sphere in a quiescent matrix has received much attention as an experimental method for measuring the interfacial tension [43–46]. This is a good benchmark problem for us for two reasons. First, the retraction is driven only by the interfacial tension. Thus, it is a sensitive test on how accurately our 3D algorithm resolves the interfacial layer and computes the interfacial force. Second, the geometry is axisymmetric, and we can compare the 3D results to high-accuracy 2D axisymmetric results. Figure 2 shows the portion of the computational domain that contains the drop. Because of symmetry only one-eighth of the physical domain needs to be computed. The size of the domain is $5R_0 \times 5R_0 \times 5R_0$ where R_0 is the radius of the undeformed drop. The drop is located at the center of the physical domain, which is at one corner of the computational domain. We used symmetry conditions (zero normal velocity and zero shear stress) on the three coordinate planes, and stress-free conditions on the far-field boundaries. Initially, the major and minor axis of the drop are $a = 1.5625R_0$ and $b = c = 0.80R_0$. In drop retraction experiments, the fluids are typically highly viscous and the retraction

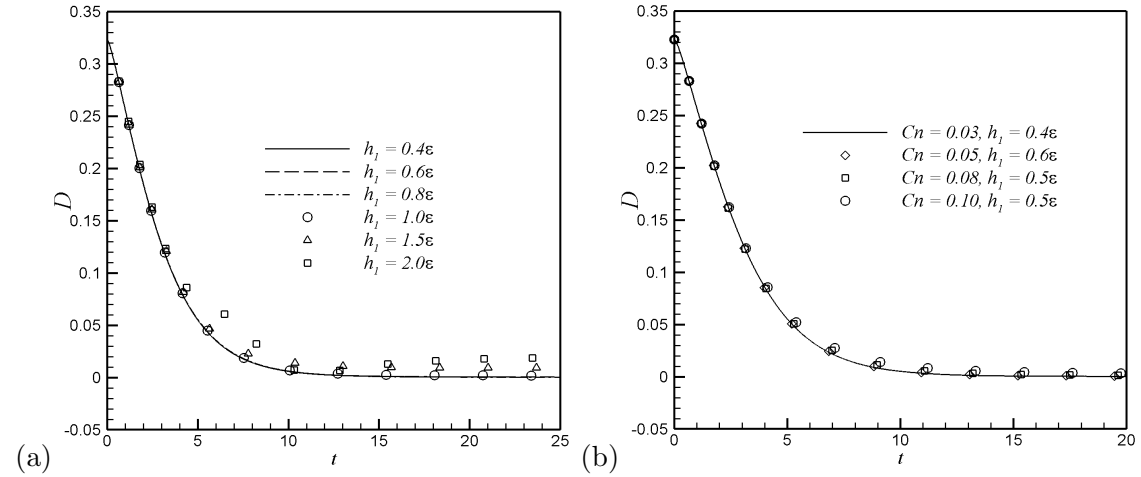

Figure 3: Retraction of an elongated drop computed using AMPHI3D. (a) Convergence with respect to mesh resolution at $Cn = 0.05$. The three lines practically overlap. (b) Convergence with respect to the interfacial thickness in the diffuse-interface model. Time is scaled by $\mu_m R_0/\sigma$, and the viscosity ratio $\beta = 1$.

speed is very low. Thus, we have neglected inertia in our computations. Since there is no externally imposed velocity in the problem, the only time scale is the capillary time $t_c = \mu_m R_0/\sigma$. Three dimensionless parameters may be constructed: the viscosity ratio $\beta = \mu_d/\mu_m$, with the subscripts d and m denoting the drop and matrix respectively, the Cahn number $Cn = \epsilon/R_0$ that indicates how thin the diffuse interface is, and the Peclet number $Pe = \sigma R_0 \epsilon^2/(\mu_d \gamma \lambda)$ that indicates the magnitude of the Cahn-Hilliard diffusion.

As alluded to at the beginning, an accurate diffuse-interface solution requires that the interface be thin enough to approximate the sharp-interface limit, and that the thin interface be resolved by a sufficient number of grid points. These conditions may be called, respectively, model convergence and mesh convergence. For the mesh convergence tests, we fix the Cahn number $Cn = 0.05$ and vary the interfacial mesh size h_1 by tuning the parameter C in Eq. (19). The bulk mesh sizes h_2 and h_3 are fixed at $0.35R_0$ and $0.9R_0$, as further refinement produces no visible change in the results. To confirm model convergence, we vary the Cahn number down to 0.03. Figure 3 depicts the retraction of the elongated drop, in terms of the relaxation of the drop deformation parameter $D = (a-b)/(a+b)$, computed using different Cn and h_1 values. Figure 3(a) shows that mesh convergence is achieved when the interfacial grid size h_1 is less than or equal to the capillary width ϵ. This is similar to

the criterion in 2D simulations [20] for various flow conditions. Figure 3(b) demonstrates that the model prediction converges to the sharp-interface limit when $Cn \leq 0.05$. This is a surprisingly lax criterion; the value 0.05 is not only much larger than for typical physical problems with real interfaces, but is above the critical value ($Cn \sim 0.01$) previously determined for 2D simulations [20]. The reason is that the retraction is a very mild flow that does not stretch and distort the interfacial profile strongly. In more severe flow situations, such as drop deformation in an elongational flow (see subsection III.B below), model convergence requires a more stringent threshold.

Once the sharp-interface limit is achieved, the mobility γ and the Peclet number Pe matter little to the results. For instance, we have varied Pe between 2357 and 9428 in Fig. 3, with virtually no effects on the model-converged simulations. This is because the ϕ profile remains at the equilibrium state when the interface becomes sufficiently thin. As long as the correct interfacial tension is produced, details of the Cahn-Hilliard diffusion within the thin interface are irrelevant to the retraction of the drop. This contrasts the drop spreading problem in subsection III.C, where the speed of the moving contact line is determined by the magnitude of Cahn-Hilliard diffusion.

Now that we established the thresholds for model and mesh convergence, we study the effect of the viscosity ratio β on drop retraction, and compare the results with 2D axisymmetric simulations and experimental data. Both ϵ and h_1 are assigned $0.03R_0$, which implies $Cn = 0.03$. The other two grid sizes are $h_2 = 0.35R_0$ inside the drop and $h_3 = 0.9R_0$ in the matrix. The generated mesh has 194,829 tetrahedra and 35,910 vertices. The computational results are shown in Fig. 4 for three β values. The drop retracts more quickly for lower β. Note that time is scaled by the capillary time $t_c = \mu_m R_0/\sigma$ based on the matrix viscosity. The effect of β implies that the retraction is slowed down by drop-phase viscosity, which is not surprising. For the moderate β values tested, much of the retraction occurs within several t_c. Since the process is governed by the competition between interfacial tension and viscosity, t_c is indeed the proper time scale. Besides, we have carried out 2D axisymmetric computations using the same geometric and physical parameters. The agreement between 2D and 3D computations is excellent for all three β values; this may be taken as a validation of the accuracy of the 3D algorithm.

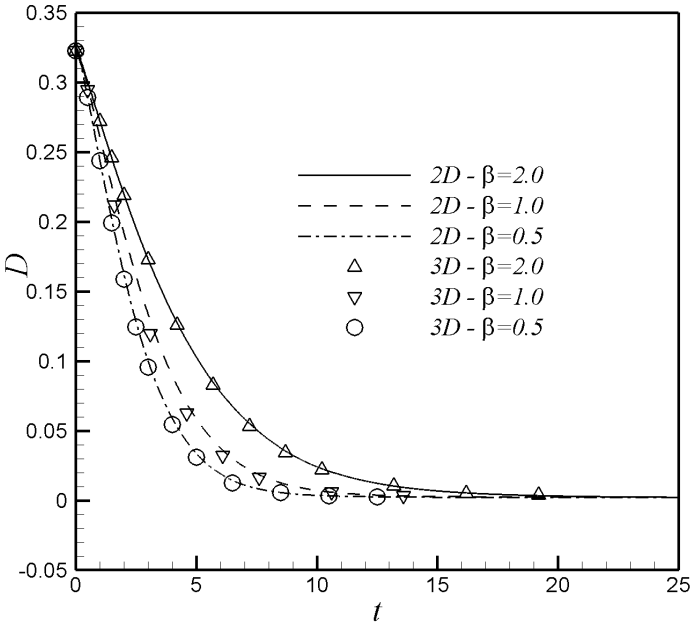

Figure 4: Comparison between 2D and 3D predictions of drop retraction for 3 different viscosity ratios. Time has been made dimensionless by the capillary time $t_c = \mu_m R_0/\sigma$.

Guido and Villone [47] measured drop retraction in Newtonian fluids, and compared the data with a small-deformation theoretical formula:

$$D = D_0 \exp\left[-\frac{40(\beta+1)}{(2\beta+3)(19\beta+16)}t\right] \tag{22}$$

where D_0 is the initial deformation parameter, and time has been made dimensionless by $t_c = \mu_m R_0/\sigma$. Equation (22) predicts an exponential relaxation of $D(t)$ as well as a particular dependence on the viscosity ratio β. Thus, the data should fall on a straight line in a semi-log plot, whose slope would then allow a straightforward calculation of the interfacial tension σ. This is the basis for using drop retraction for measuring σ. Plotting their data as $\ln D$ versus t, Guido and Villone found that the straight line prevails only after D has fallen below a value of 0.09. This is little surprise since Eq. (22) derives from a small-deformation theory. Thus, Guido and Villone [47] have taken $D_0 = 0.09$ to be the start of the exponential relaxation.

In Fig. 5, we compare our computations for 3 viscosity ratios with the experimental data of Guido and Villone [47] and the small-deformation theory (Eq. 22). Following these

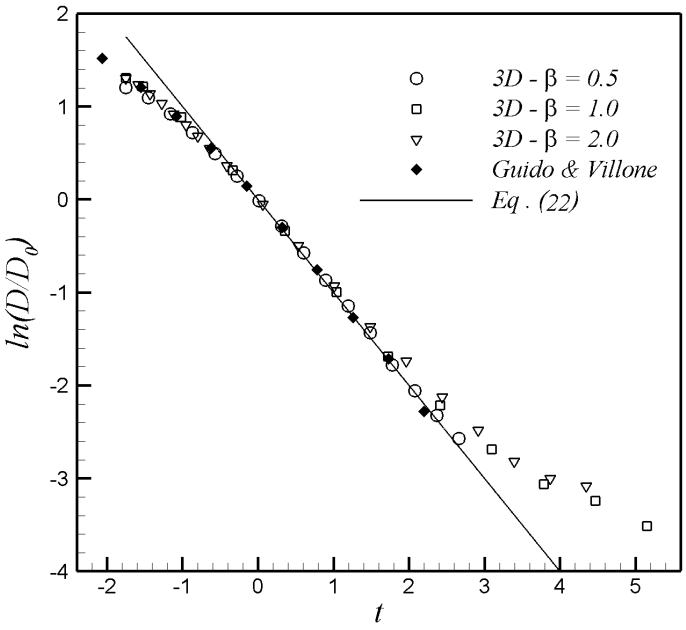

Figure 5: Drop retraction: comparison with the experimental data and the small-deformation theory [47]. Time is made dimensionless by $\frac{(2\beta+3)(19\beta+16)}{40(\beta+1)}\frac{\mu_m R_0}{\sigma}$, and its origin has been shifted to the moment when the instantaneous deformation parameter $D = 0.09$ to be consistent with the experimental data.

authors, we have shifted the origin of time to when D falls to the threshold of 0.09, and rescaled time by the viscosity ratio β according to the formula. Three interesting observations can be made. First, the numerical results for $\beta = 0.5$, 1 and 2 collapse almost perfectly onto a single master curve. Thus, the dependence of drop retraction on β is precisely as prescribed by Eq. (22); this is true even for the initial stage of retraction where D is large and the equation is not expected to hold. Second, there is excellent agreement between our numerical results and the experimental data in the range where the two overlap, down to $\ln(D/D_0) \approx -2$. This provides another validation for AMPHI3D. Finally, our data fall on the straight line representing Eq. (22) only for an intermediate range. The initial stage, as explained above, deviates from the formula because D is too large. However, toward the end of the retraction ($\ln(D/D_0) < -2$), our results again show slower retraction than the theoretical prediction. This is a numerical artifact due to inadequate mesh resolution. By this time, the drop is nearly spherical ($D \approx 1.2 \times 10^{-2}$); its surface deviates from the perfect sphere by less than the grid size. Thus it becomes difficult to compute the interfacial motion

accurately. Therefore, Fig. 5 has validated the diffuse-interface model and the AMPHI3D algorithm, but in the meantime indicated the limit of the code in terms of mesh resolution.

B. Drop deformation under elongation

The purpose of this subsection is to explore the effect of the Cahn number Cn in a stronger flow than drop retraction. By comparison with 2D axisymmetric results, we establish the upper limit of Cn for acceptable results. This is a fundamental issue with diffuse-interface simulations, which typically use an artificially large capillary width ϵ. It is only after ϵ and the Cahn number Cn fall below threshold values that the results no longer depends on ϵ, and the numerical simulation has converged to the sharp-interface limit. In our prior 2D calculations, the threshold Cn for such model convergence is typically of order 10^{-2}. For each ϵ, one must ensure that the grid is sufficiently fine to achieve mesh convergence. Prior 2D computations [20] showed that the size of the fine grid at the interface should be $h_1 = \epsilon$ or smaller. This has been confirmed for 3D computations as well (cf. Fig. 3b). So we will focus on the effect of Cn in the following.

For a drop deforming in a uniaxial extensional flow, the computational domain is similar to that in Fig. 2. The domain size is $6R_0 \times 5R_0 \times 5R_0$, R_0 being the radius of the undeformed drop, with symmetry boundary conditions on the coordinate planes $x = 0$, $y = 0$ and $z = 0$. The uniaxial elongational flow condition is applied on the other 3 boundary planes at $x = 6R_0$, $y = 5R_0$ and $z = 5R_0$, on which the velocity is prescribed as $(u, v, w) = (\dot{\epsilon}x, -\dot{\epsilon}y/2, -\dot{\epsilon}z/2)$, $\dot{\epsilon}$ being the elongational rate. For the initial condition, we start with zero-velocity inside the domain and apply the prescribed velocities on the boundaries. Similar to the drop retraction simulation, we neglect inertia. Then the physical problem is determined by two dimensionless parameters: the viscosity ratio β and the capillary number:

$$Ca = \frac{\mu_m \dot{\epsilon} R_0}{\sigma}, \tag{23}$$

where μ_m is the matrix viscosity and σ is the interfacial tension. For simplicity, we assign equal viscosity to the drop and the matrix so $\beta = 1$.

Figure 6 compares our 3D numerical results for $Cn = 0.02$ and 0.03 with 2D axisymmetric results with $Cn = 0.02$ and 0.01 previously published by Yue *et al.* [20]. Drop deformation is indicated by the ratio of the drop length L to its initial radius R_0. The

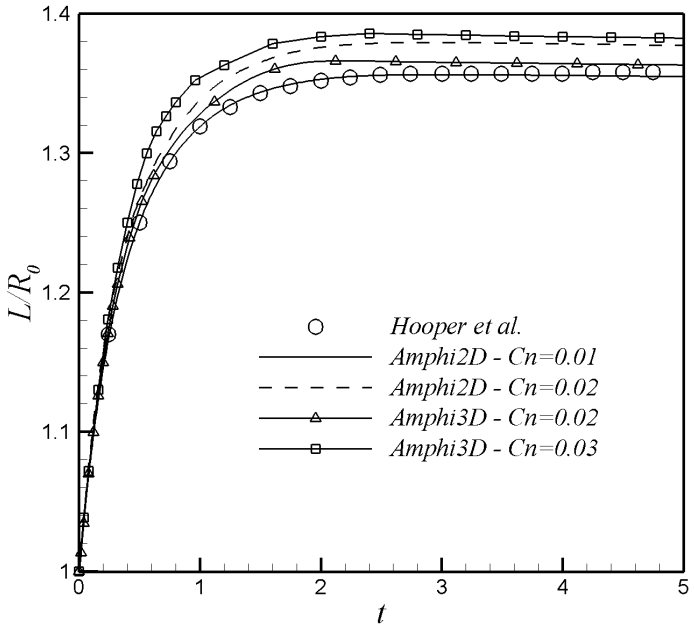

Figure 6: Drop deformation under elongational flow: comparison of AMPHI3D computation at different Cahn numbers with 2D axisymmetric computations of Yue *et al.* [20] and Hooper *et al.* [48] The other parameters are $\beta = 1$, $Ca = 0.1$, $h_1 = \epsilon$, and $Pe = 18856\,Cn$.

results of Hooper *et al.* [48], using a moving-grid finite-element scheme, is also shown. The general trend is the same among the five simulations, but there are small quantitative differences. As Cn is reduced from 0.03 to 0.02, the steady-state deformation decreases by 5% in our 3D computation. This is comparable to previous convergence studies on the 2D version of AMPHI [20], reproduced in Fig. 6. Thus, $Cn = 0.02$ is considered the threshold in our context for model-convergent computations. Our 3D curve at $Cn = 0.02$ is also in close agreement with the result of Hooper *et al.* [48], with the steady-state deformation within 1.3% of each other. We did not explore smaller Cn values as we did in 2D, down to $Cn = 0.01$ and smaller, because the memory and computational time become highly demanding. For $Cn = 0.02$, for example, the number of unknowns exceeds two million and the memory allocation approaches 10 GB.

The observation that larger Cn leads to somewhat larger steady-state drop deformation has been analyzed by Yue *et al.* [7] Essentially, the elongational flow convects the interfacial profile such that the interface becomes effectively thicker near the tips of the drop. This amounts to a locally reduced interfacial tension, which scales with λ/ϵ, and tends to increase

the steady state L. This effect is more prominent for thicker interfaces, and become negligible as the sharp interface is approached. This also explains why the model-convergence criterion here is more stringent than that for drop retraction. In the latter, the flow induced by the retraction is weak and does not distort the interfacial profile as much. Thus, the interfacial tension can be captured accurately with a thicker interface.

C. Drop spreading on partially wetting substrate

In this subsection, we consider a drop spreading on a partially wetting substrate. The most important physics here is the motion of the contact line, which presents a well-known stress singularity that is conventionally removed by assuming ad hoc conditions such as Navier slip or numerical slip [49,50]. In recent years, the diffuse-interface model has emerged as a promising alternative that offers a more rational approach to this issue [33, 51–53]. While the Cahn-Hilliard dynamics is typically used as a device for capturing the moving interface, the diffusion across the interface also offers a means to regularize the stress singularity within the classical no-slip framework. The question is whether the Cahn-Hilliard diffusion adequately represents the true physics at the contact line. Yue *et al.* [14] have offered an affirmative answer by showing that the Cahn-Hilliard model approaches a sharp interface limit when the capillary width $\epsilon \to 0$ while the molecular mobility γ and other model parameters are kept constant, and that the model can predict experimental data quantitatively if relaxation of wall layers is considered. This suggests that the phase-field model may be a useful tool for computing complex flows involving contact lines. In studying the spread of a drop, our main objective here is to validate AMPHI3D by comparing its predictions with 2D axisymmetric computations and experiments. Besides, we will also examine physically interesting questions such as the effect of wettability on the speed of spreading. With a moving contact line, model convergence to the sharp-interface limit is a subtler affair that depends not only on Cn but also on the mobility γ and the viscosities of the components [14]. For the parameters used in this subsection, $Cn = 0.03$ and 0.04 are sufficiently small.

Figure 7 depicts the spreading of a drop with a static contact angle of $\theta_s = 60^\circ$. The surrounding fluid has the same viscosity as the drop phase, and inertia is neglected. We also neglect gravity so the spreading is driven solely by interfacial forces. We start with a

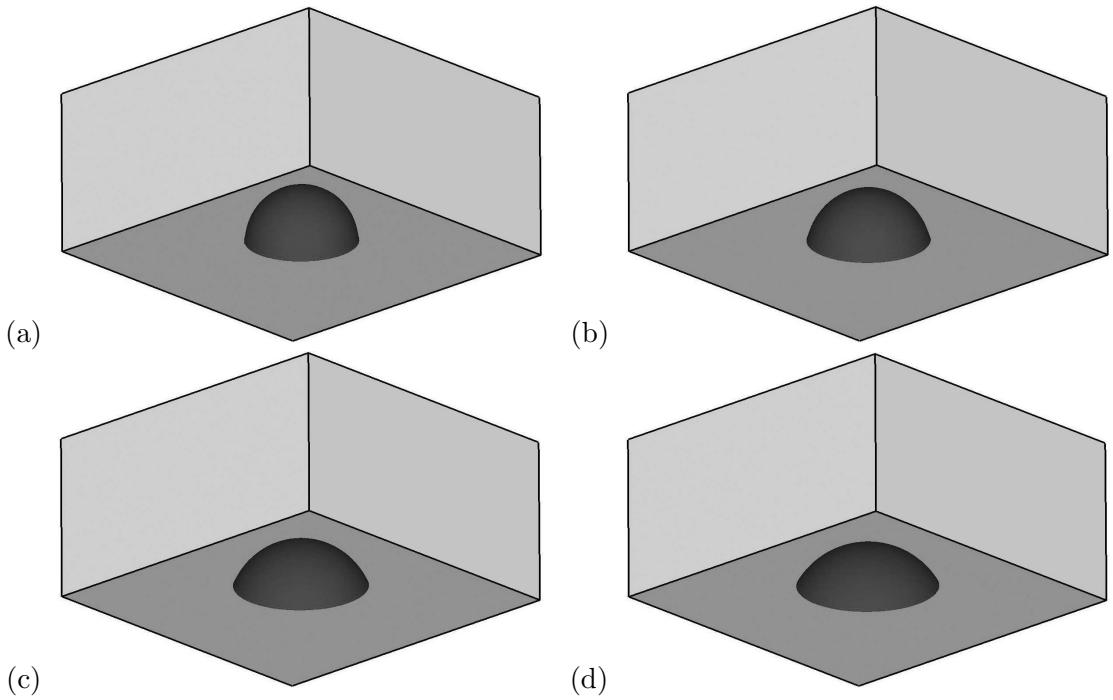

Figure 7: The evolution of drop spreading on a substrate with static contact angle of 60°. (a) $t = 0$, (b) $t = 5.50$, (c) $t = 20.5$, (d) $t = 145.5$. Time is scaled by $t_c = \mu_m R_0/\sigma$, where R_0 is the radius of the initial hemisphere. $Cn = 0.03$, $h_1 = \epsilon$, $Pe = 2828$.

hemispherical drop on a substrate, with an initial contact angle of 90° (Fig. 7a). In time, the drop spreads out on the substrate, and approaches a steady state of a spherical cap with the prescribed contact angle $\theta_s = 60°$ (Fig. 7d).

The effect of θ_s on the spreading process is demonstrated by Fig. 8. The radius of the "footprint" of the drop, i.e. the circle formed by the expanding contact line, grows rapidly at the beginning, and then plateaus toward a steady-state value over a time period of more than $100t_c$ (Fig. 8a). The drop with the smaller θ_s wets the substrate better and thus spreads more rapidly at the beginning. It also produces a larger puddle at the end. The close agreement between 2D axisymmetric simulations and the 3D ones serves as another validation of the 3D code.

The temporal evolution of the apparent contact angle θ is depicted in Fig. 8(b). At $t = 0$, $\theta = 90°$ from the hemispherical initial shape. Once the drop starts to spread, the definition of θ becomes somewhat ambiguous. Following Mazouchi *et al.* [50], we define θ from the slope of the interface at the height of $0.1R_0$ above the substrate, where the

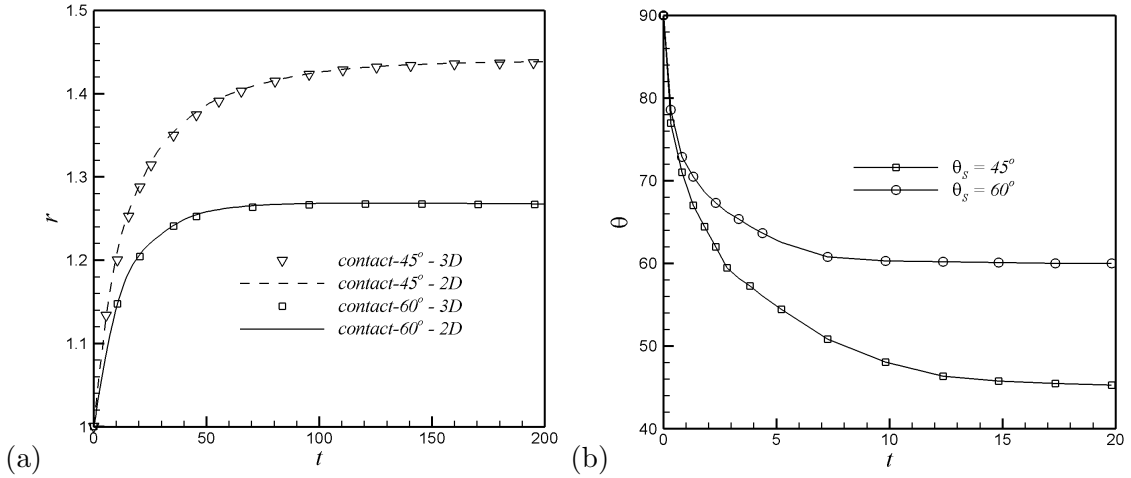

Figure 8: Effect of the static contact angle θ_s on drop spreading. (a) Growth of the radius of the "footprint" of the drop in time. 3D and 2D axisymmetric results are in excellent agreement. (b) Relaxation of the apparent contact angle θ toward θ_s. Though not plotted, the 2D results for θ essentially overlap the 3D curves. The other parameters are the same as in Fig. 7

interface is more or less a straight line. The need for such a subjectively defined quantity is due to the difficulty in determining the so-called "microscopic contact angle" right on the substrate. Experimentally, the latter cannot be measured, and one necessarily records the interface some small distance above the substrate. In our diffuse-interface computation, the local phase field is dynamically perturbed by the flow near the moving, non-equilibrium contact line. Thus, the local orientation of the ϕ contours may not reflect the interfacial orientation in the physically sense [13]. As expected, θ relaxes toward θ_s, and more rapidly for the more wetting drop for which the initial contact angle of 90° constitutes a greater deviation from the minimum energy equilibrium state. Owing to its definition, the apparent contact angle θ is slightly below θ_s at the end of the spread.

Drop spreading on a substrate with partial wetting condition has been studied previously by many researchers. For example, Zosel [54] measured the spreading of drops of polymer solutions on a partially wetting substrate. Khatavkar *et al.* [52] simulated the capillary spreading of Newtonian droplets using the diffuse interface method in 2D axisymmetric geometry, and compared the numerical results with Zosel's experiment. For comparison, we have simulated the same problem in 3D using the same parameters.

Figure 9 plots the increasing radius $r(t)$ of the contact line for the three studies. The initial condition differs from that in Fig. 7(a) in that a full spherical drop is deposited on the

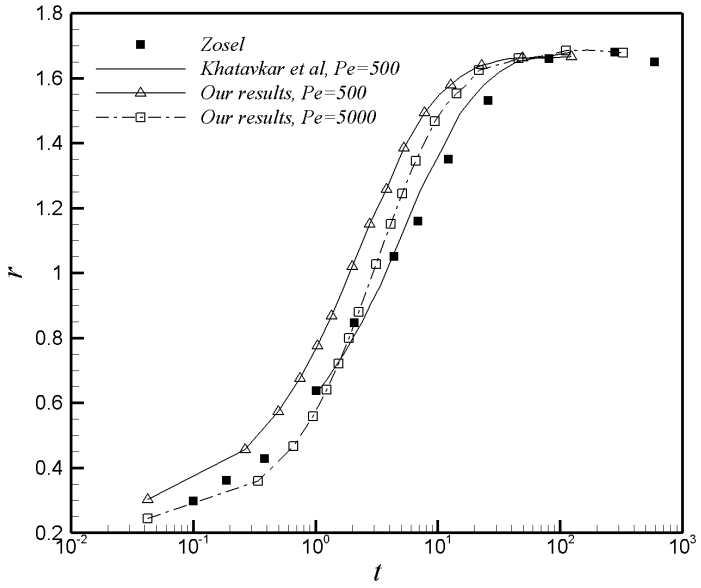

Figure 9: Comparison of our drop spreading simulations with the experiment of Zosel [54] and the diffuse-interface computation of Khatavkar *et al.* [52]. The static contact angle $\theta_S = 56^\circ$ for all results. $Cn = 0.04$ and $\beta = 100$ in both our computations and that of Khatavkar *et al.* Time has been made dimensionless by the capillary time $\mu_d R_0/\sigma$, R_0 being the radius of the spherical drop at the start.

substrate, which then proceeds to spread. In the experiment, the viscosity ratio β exceeds 10^3. Such values make numerical convergence difficult in diffuse-interface computations. The numerical experiments of Khatavkar *et al.* showed that as β gets as large as 100, the result becomes very insensitive to β, and they compared numerical results for $\beta = 100$ with the experiment of Zosel [54]. We will do the same by using $\beta = 100$. The static contact angle $\theta_s = 56^\circ$ in the experiment is implemented in the computations, and we use the same $Cn = 0.04$ as Khatavkar *et al.* The mobility parameter γ in the Cahn-Hilliard equation cannot be easily related to experimental values. Khatavkar *et al.* found that good fit with the experimental data can be obtained using a γ that corresponds to a Peclet number $Pe = 500$. In our 3D computations, the spreading at $Pe = 500$ occurs faster than the experimental data and the axisymmetric result of Khatavkar *et al.* Instead, reasonable agreement with the experiment is obtained for a larger $Pe = 5000$. The larger Pe or smaller γ reduces the Cahn-Hilliard diffusion at the contact line, and slows down its motion. The reason for the discrepancy between the two computations is not clear at present. The qualitative trend is the same in all 3 studies. The droplet spreads quickly when it initially

touches the substrate ($t < 1$). In this stage, the upper part of the drop hardly deforms; the bottom of the drop opens up and spreads rapidly. After that, there is a roughly logarithmic regime ($1 < t < 10$) during which the drop spreads against the viscous force. In the end, the drop slowly approaches the steady state.

D. Viscoelastic effects on drop retraction

We have also studied the effect of viscoelasticity in the 3D code by simulating a viscoelastic drop retracting from an elongated shape in a Newtonian medium. The geometric setup is the same as the one with the Newtonian system in III.A. The viscoelastic fluid is represented by the Oldroyd-B model [31] based on a dilute suspension of elastic dumbbells in a Newtonian solvent. Yue *et al.* [6] have simulated retraction of Oldroyd-B drops in a Newtonian matrix in planar 2D geometry. The main finding is that a viscoelastic drop initially retracts faster than a Newtonian one having the same steady-shear viscosity, but eventually falls behind and returns to the spherical shape in longer time than its Newtonian counterpart. The purpose of the current simulations is two-fold. The first is to validate the 3D code using 2D axisymmetric simulations. The second is to confirm the physical effects of viscoelasticity on drop retraction previously observed in 2D planar calculations.

The magnitude of viscoelasticity is customarily represented by a Deborah number, the ratio between the polymer relaxation time and a flow time. For a drop retracting in a quiescent fluid, the only time scale is the capillary time $t_c = \mu_m R_0/\sigma$, and thus our Deborah number is defined as

$$De = \frac{\lambda_H \sigma}{\mu_m R_0}. \tag{24}$$

We set the polymer viscosity μ_p to be equal to the solvent viscosity μ_s, so that the retardation-relaxation time ratio is 0.5. We compare the viscoelastic drop retraction with that of a Newtonian drop whose viscosity μ_d matches the total viscosity $\mu_p + \mu_s$. In both cases, this is also the viscosity of the suspending Newtonian medium. Using these physical parameters, we have done the 3D computation using 3 grids that differ in the mesh size h_2 inside the drop. The results are compared with the 2D axisymmetric computation and the Newtonian result in Fig. 10.

First, convergence with mesh refinement within the drop is evident from the fact that the 3D curves approach the 2D axisymmetric one with decreasing h_2. In this problem, a

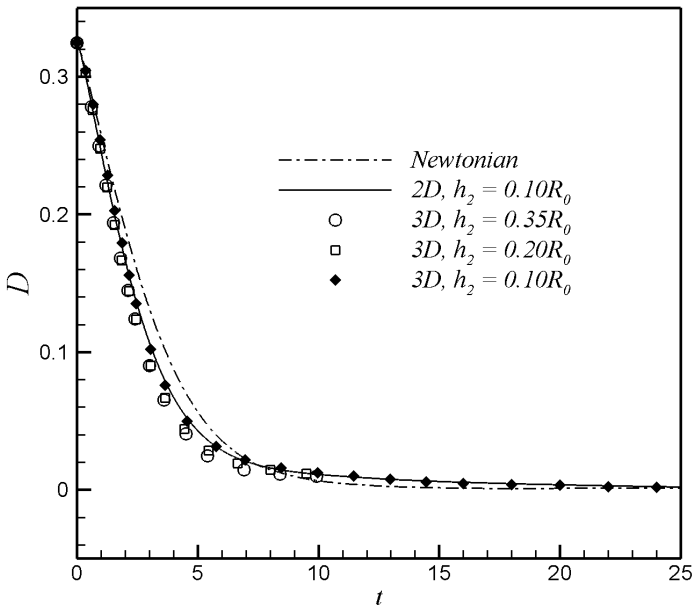

Figure 10: Retraction of a viscoelastic drop from a spheroidal initial shape with $D_0 = 0.323$. $Cn = 0.03$, $De = 10$. Time t has been made dimensionless by $t_c = \mu_m R_0/\sigma$. The 3D viscoelastic computations have been done on three grids that have the same interfacial mesh size $h_1 = \epsilon = 0.03R_0$ and far-field mesh size $h_3 = R_0$ in the matrix, but different mesh size inside the drop: $h_2 = 0.35R_0$, $0.2R_0$ and $0.1R_0$. The 3D Newtonian run uses $h_2 = 0.2R_0$ and the 2D axisymmetric viscoelastic run has $h_2 = 0.1R_0$, both having the same h_1 and h_3 given above.

sufficiently fine h_2 is important for resolving the viscoelastic stress field inside the drop. Moreover, the threshold for mesh convergence, $h_2 = 0.1R_0$, is more stringent than its Newtonian counterpart (e.g., $h_2 = 0.35R_0$ in subsection III.A). This is probably because the viscoelastic stress tensor is discretized on piecewise linear P1 elements while the velocity uses P2 elements. Second, the viscoelastic drop retracts faster initially than the Newtonian one, but approaches the spherical shape more slowly in the end. This is qualitatively the same as previously shown in 2D planar geometry [6]. The underlying mechanism is the development of the viscoelastic stress inside the drop. As the drop starts to retract, the flow inside causes the polymer elastic stress to grow from zero on the time scale of the relaxation time λ_H. Thus, for $t < \lambda_H$, the retraction of the viscoelastic drop is faster than that of the Newtonian drop since the polymer stress has yet to develop fully. After that, the elastic stress grows to such an extent that the total stress surpasses its counterpart in the viscous Newtonian drop. The retraction of the viscoelastic drop, as a result, is hampered by the developed elastic stress for $t > \lambda_H$. For the viscoelastic drop in Fig. 10, the Deborah

number $De = 10$ implies $\lambda_H = 10t_c$. The crossover between the Newtonian and viscoelastic curves at $7.5t_c = 0.75\lambda_H$ may be taken as a rough corroboration of the above argument. Of course, the level of stress inside the drop correlates more with the instantaneous speed of retraction than with D. Thus, the crossover in D does not precisely correspond to a crossover in the internal stresses.

IV. CONCLUSION

This paper describes AMPHI3D, a 3D finite-element algorithm for simulating two-component rheologically complex fluids using a diffuse-interface formulation. A generalization of our previous 2D work, this code features an implicit solver for the Navier-Stokes and Cahn-Hilliard equations and a versatile adaptive meshing scheme that allows adequate resolution of the interfacial region at relatively low computational cost.

We have applied AMPHI3D to four benchmark problems: the retraction of an elongated viscous drop in a quiescent fluid, the deformation of a drop in a uniaxial extensional flow, the spread of a drop on a partially wetting substrate, and the retraction of a viscoelastic Oldroyd-B drop. In each case, we have used numerical and experimental results in the literature to verify AMPHI3D computations. Since all four problems have axisymmetry, we have also used 2D axisymmetric computations as benchmarks. This procedure has established the critical interfacial thickness for proper convergence of the diffuse-interface model to the sharp-interface limit, as well as the level of grid refinement that ensures adequate spatial resolution. For parameters within these limits, AMPHI3D simulations are in excellent agreement with the benchmark results. This serves as a validation of the theoretical model and the numerical algorithm.

The focus of this work is on the AMPHI3D methodology rather than detailed exploration of the physics involved. But it is clear that this code can be fruitfully applied to many interesting problems that are beyond the reach of two-dimensional studies. One limitation for the current package, however, is that it is a single-processor serial code. For large-scale problems, the coupled solution of the Navier-Stokes and Cahn-Hilliard equations requires a large memory. Parallelization may help expand its capacity for large-scale 3D computations.

Acknowledgment: Acknowledgment is made to the Donors of The Petroleum Research Fund, administered by the American Chemical Society, for partial support of this research. J.J.F. was also supported by the Canada Research Chair program, NSERC, CFI and NSFC (Grant Nos. 50390095, 20674051). C.Z. acknowledges partial support by a University Graduate Fellowship from UBC and a Pacific Century Graduate Scholarship from the government of British Columbia.

References

[1] M. Joanicot, A. Ajdari, Droplet control for microfluidics, Science 309 (2005) 887–888.

[2] J. A. Sethian, P. Smereka, Level set methods for fluid interfaces, Ann. Rev. Fluid Mech. 35 (2003) 341–372.

[3] X. Y. Xie, L. C. Musson, M. Pasquali, An isochoric domain deformation method for computing steady free surface flows with conserved volumes, J. Comput. Phys. 226 (2007) 398–413.

[4] N. Aggarwal, K. Sarkar, Deformation and breakup of a viscoelastic drop in a Newtonian matrix under steady shear, J. Fluid Mech. 584 (2007) 1–21.

[5] P. Yue, J. J. Feng, C. A. Bertelo, H. H. Hu, An arbitrary Lagrangian-Eulerian method for simulating bubble growth in polymer foaming, J. Comput. Phys. 226 (2007), 2229–2249.

[6] P. Yue, J. J. Feng, C. Liu, J. Shen, Diffuse-interface simulations of drop coalescence and retraction in viscoelastic fluids, J. Non-Newtonian Fluid Mech. 129 (2005) 163–176.

[7] P. Yue, J. J. Feng, C. Liu, J. Shen, A diffuse-interface method for simulating two-phase flows of complex fluids, J. Fluid Mech. 515 (2004) 293–317.

[8] J. J. Feng, C. Liu, J. Shen, P. Yue, An energetic variational formulation with phase field methods for interfacial dynamics of complex fluids: advantages and challenges, In M.-C. T. Calderer, E. M. Terentjev, editors, Modeling of Soft Matter, pages 1–26. Springer, New York, 2005.

[9] P. Lin, C. Liu, Simulations of singularity dynamics in liquid crystal flows: A C-0 finite element approach, J. Comput. Phys. 215 (2006) 348–362.

[10] P. Lin, C. Liu, H. Zhang, An energy law preserving C-0 finite element scheme for simulating the kinematic effects in liquid crystal dynamics, J. Comput. Phys. 227 (2007) 1411–1427.

[11] P. Yue, J. J. Feng, C. Liu, J. Shen, Interfacial force and Marangoni flow on a nematic drop retracting in an isotropic fluid, J. Colloid Interface Sci. 290 (2005) 281–288.

[12] C. Zhou, P. Yue, J. J. Feng, Formation of simple and compound drops in microfluidic devices, Phys. Fluids 18 (2006) 092105.

[13] L. M. Pismen, Nonlocal diffuse interface theory of thin films and the moving contact line, Phys. Rev. E 64 (2001) 021603.

[14] P. Yue, C. Zhou, J. J. Feng, Sharp interface limit of the Cahn-Hilliard model for moving contact lines, J. Fluid Mech. (in press), 2009.

[15] J. Lowengrub, L. Truskinovsky, Quasi-incompressible Cahn-Hilliard fluids and topological transitions, Proc. Roy. Soc. Lond. A 454 (1998) 2617–2654.

[16] D. Jacqmin, Calculation of two-phase Navier-Stokes flows using phase-field modelling, J. Comput. Phys. 155 (1999) 96–127.

[17] B. J. Keestra, P. C. J. van Puyvelde, P. D. Anderson, H. E. H. Meijer, Diffuse interface modeling of the morphology and rheology of immiscible polymer blends, Phys. Fluids 15 (2003) 2567–2575.

[18] V. E. Badalassi, H. D. Ceniceros, S. Banerjee, Computation of multiphase systems with phase field model, J. Comput. Phys. 190 (2003) 371–397.

[19] G. Caginalp, X. Chen, Convergence of the phase field model to its sharp interface limits, Euro. J. Appl. Math. 9 (1998) 417–445.

[20] P. Yue, C. Zhou, J. J. Feng, C. F. Ollivier-Gooch, H. H. Hu, Phase-field simulations of interfacial dynamics in viscoelastic fluids using finite elements with adaptive meshing, J. Comput. Phys. 219 (2006) 47–67.

[21] P. Yue, C. Zhou, J. J. Feng, A computational study of the coalescence between a drop and an interface in Newtonian and viscoelastic fluids, Phys. Fluids 18 (2006) 102102.

[22] C. Zhou, P. Yue, J. J. Feng, Simulation of neutrophil deformation and transport in capillaries using simple and compound drop models, Ann. Biomed. Eng. 35 (2007) 766–780.

[23] C. Zhou, P. Yue, J. J. Feng, The rise of Newtonian drops in a nematic liquid crystal, J. Fluid Mech. 593 (2007) 385–404.

[24] C. Zhou, P. Yue, J. J. Feng, Dynamic simulation of droplet interaction and self-assembly in a nematic liquid crystal, Langmuir 24 (2008) 3099–3110.

[25] D. Jacqmin, Onset of wetting failure in liquid-liquid systems, J. Fluid Mech. 517 (2004) 209–228.

[26] D. D. Joseph, Lubricated pipelining, Powder Technol. 94 (1997) 211–215.

[27] P. Yue, C. Zhou, J. Dooley, J. J. Feng, Elastic encapsulation in bicomponent stratified flow of viscoelastic fluids, J. Rheol. 52 (2008) 1027–1042.

[28] D. M. Anderson, G. B. McFadden, A. A. Wheeler, Diffuse-interface methods in fluid mechanics, Ann. Rev. Fluid Mech. 30 (1998) 139–165.

[29] C. Zhou, P. Yue, J. J. Feng, C. Liu, J. Shen, Heart-shaped bubbles rising in anisotropic liquids, Phys. Fluids 19 (2007) 041703.

[30] C. Zhou, P. Yue, J. J. Feng, Dynamic simulation of capillary breakup of nematic fibers: molecular orientation and interfacial rupture, J. Comput. Theor. Nanosci. (accepted), 2009.

[31] R. B. Bird, C. F. Curtiss, R. C. Armstrong, O. Hassager, Dynamics of Polymeric Liquids, Vol. 2. Kinetic Theory, Wiley, New York, 1987.

[32] J. W. Cahn, J. E. Hilliard, Free energy of a nonuniform system. I. interfacial free energy, J. Chem. Phys. 28 (1958) 258–267.

[33] D. Jacqmin, Contact-line dynamics of a diffuse fluid interface, J. Fluid Mech. 402 (2000) 57–88.

[34] J. W. Cahn, Critical-point wetting, J. Chem. Phys. 66 (1977) 3667–3672.

[35] J. Shen, Efficient spectral-Galerkin method. II. direct solvers of second and fourth order equations by using Chebyshev polynomials, SIAM J. Sci. Comput. 16 (1995) 74–87.

[36] H. H. Hu, N. A. Patankar, M. Y. Zhu, Direct numerical simulations of fluid-solid systems using the arbitrary Lagrangian-Eulerian technique, J. Comput. Phys. 169 (2001) 427–462.

[37] H. Gan, J. J. Feng, H. H. Hu, Simulation of the sedimentation of melting solid particles, Int. J. Multiphase Flow 29 (2003) 751–769.

[38] L. A. Freitag, C. F. Ollivier-Gooch, Tetrahedral mesh improvement using swapping and smoothing, Int. J. Numer. Methods Eng. 40 (1997) 3979–4002.

[39] C. F. Ollivier-Gooch, C. Boivin, Guaranteed-quality simplical mesh generation with cell size and grading control, Engineering with Computers 17 (2001) 269–286.

[40] C. Boivin, C. F. Ollivier-Gooch, Guaranteed-quality triangular mesh generation for domains with curved boundaries, Int. J. Numer. Methods Eng. 55 (2002) 1185–1213.

[41] J. R. Shewchuk, Delaunay Refinement Mesh Generation, PhD thesis, Carnegie Mellon University, 1997.

[42] D. F. Watson, Computing the n-dimensional Delaunay tessellation with application to Voronoi polytopes, Comput. J. 24 (1981) 167–172.

[43] H. Mo, C. Zhou, W. Yu, A new method to determine interfacial tension from the retraction of ellipsoidal drops, J. Non-Newtonian Fluid Mech. 91 (2000) 221–232.

[44] Y. Son, K. B. Migler, Interfacial tension measurement between immiscible polymers: Improved deformed drop retraction method, Polymer 43 (2002) 3001–3006.

[45] S. Velankar, H. Zhou, H. K. Jeon, C.W. Macosko, CFD evaluation of drop retraction methods for the measurement of interfacial tension of surfactant-laden drops, J. Colloid Interface Sci. 272 (2004) 172–185.

[46] V. E. Ziegler, B. A. Wolf, Interfacial tensions from drop retraction versus pendant drop data and polydispersity effects, Langmuir 20 (2004) 8688–8692.

[47] S. Guido, M. Villone, Measurement of interfacial tension by drop retraction analysis, J. Colloid Interface Sci. 209 (1999) 247–250.

[48] R. W. Hooper, V. F. de Almeida, C. W. Macosko, J. J. Derby, Transient polymeric drop extension and retraction in uniaxial extensional flows, J. Non-Newtonian Fluid Mech. 98 (2001) 141–168.

[49] M. Renardy, Y. Renardy, J. Li, Numerical simulation of moving contact line problems using a volume-of-fluid method, J. Comput. Phys. 171 (2001) 243–263.

[50] A. Mazouchi, C. M. Gramlich, G. M. Homsy, Time-dependent free surface Stokes flow with a moving contact line. I. Flow over plane surfaces, Phys. Fluids 16 (2004) 1647–1659.

[51] W. Villanueva, G. Amberg, Some generic capillary-driven flows, Int. J. Multiphase Flow 32 (2006) 1072–1086.

[52] V. V. Khatavkar, P. D. Anderson, H. E. H. Meijer, Capillary spreading of a droplet in the partially wetting regime using a diffuse-interface model, J. Fluid Mech. 572 (2007) 367–387.

[53] H. Ding, P. D. M. Spelt, Inertial effects in droplet spreading: a comparison between diffuse-interface and level-set simulations, J. Fluid Mech. 576 (2007) 287–296.

[54] A. Zosel, Studies of the wetting kinetics of liquid drops on solid surfaces, Colloid Polym. Sci. 271 (1993) 680–687.